Soft modes near the buckling transition of icosahedral shells

M. Widom

Department of Physics, Carnegie Mellon University, Pittsburgh, Pennsylvania 15213, USA
and Department of Computational Biology, University of Pittsburgh, School of Medicine, Pittsburgh, Pennsylvania 15260, USA

J. Lidmar

Department of Physics, Royal Institute of Technology, AlbaNova, SE-106 91 Stockholm, Sweden

David R. Nelson

Department of Physics, Harvard University, Cambridge, Massachusetts 02139, USA

Icosahedral shells undergo a buckling transition as the ratio of Young's modulus to bending stiffness increases. Strong bending stiffness favors smooth, nearly spherical shapes, while weak bending stiffness leads to a sharply faceted icosahedral shape. Based on the phonon spectrum of a simplified mass-and-spring model of the shell, we interpret the transition from smooth to faceted as a soft-mode transition. In contrast to the case of a disclinated planar network where the transition is sharply defined, the mean curvature of the sphere smooths the transition. We define elastic susceptibilities as the response to forces applied at vertices, edges, and faces of an icosahedron. At the soft-mode transition the vertex susceptibility is the largest, but as the shell becomes more faceted the edge and face susceptibilities greatly exceed the vertex susceptibility. Limiting behaviors of the susceptibilities are analyzed and related to the ridge-scaling behavior of elastic sheets. Our results apply to virus capsids, liposomes with crystalline order, and other shell-like structures with icosahedral symmetry.

PACS number(s): 87.68.+z, 87.16.Dg, 46.32.+x, 68.60.Bs

I. INTRODUCTION

Virus capsids [1] and other structures such as colloidosomes [2] and liposomes [3,4] consist of thin shells of spherical topology that frequently exhibit icosahedral symmetry. A popular simplified model [5–8] replaces the shell with a triangulated network of masses and springs (see Fig. 1). This network consists of five- and six-coordinated vertices, with the five-coordinated vertices aligned with the fivefold icosahedral symmetry axes. Five-coordinated vertices may be considered as $+2\pi/6$ disclinations within an otherwise six-coordinated lattice. These disclinations are absent in conventional continuum models of spherical shells [9–11].

The elastic properties of the capsid can be mimicked by suitably adjusting the spring constants to obtain the desired Young's modulus Y and by imposing a curvature energy to obtain the bending modulus κ. Strains associated with the disclinations cause the network to buckle [12], transforming the shape from smooth and nearly spherical to strongly faceted and nearly icosahedral [5]. A dimensionless parameter controls the transformation. We define the Foppl–von Karman number

$$\gamma = \frac{YR^2}{\kappa}, \tag{1}$$

where R is the linear dimension of the shell. The buckling occurs when γ exceeds a value γ_b of order 10^2 (see Fig. 2). For the virus HK97, which appears to facet as it matures [13,14], γ reaches a value of order 10^3 according to the estimate of Ref. [5]. Varying the pH of the solution can alter γ, with the range 100–900 reported for the virus CCMV [15,16]. At much larger values of γ (in excess of 10^6), which should characterize liposomes with crystalline order, an interesting phenomenon known as "ridge scaling" emerges [17–22].

Caspar and Klug [1] classify icosahedral structures by a pair of integers (P,Q). A pair of five-coordinated vertices is connected by a path consisting of P edges in some given direction and Q edges in a direction $60°$ to the left (e.g., between two blue vertices via a red vertex in Fig. 1). The T number of the network, $T=P^2+PQ+Q^2$, gives the number of vertices as $N_v=10T+2$. There are always 12 five-coordinated vertices, so the number of six-coordinated vertices is $10(T-1)$. Structures with P and Q both nonzero and $P\neq Q$ are chiral, such that (P,Q) and (Q,P) are mirror images. Their symmetry group is the 60-element icosahedral rotation group Y. Structures with either P or $Q=0$, or with $P=Q$, are nonchiral. Their symmetry belongs to the 120-element group $Y_h=Y\times Z_2$, which should not be confused with the 120-element icosahedral double group Y' [23].

We exploit the rotational symmetry group to analyze the normal modes of the network model by diagonalizing the Hessian matrix of the elastic energy. Eigenvectors represent characteristic modes of deformation, which transform according to irreducible representations of Y, and the corresponding eigenvalues measure the mechanical stability. Because the buckling occurs in a symmetric fashion, the corresponding modes must exhibit full icosahedral symmetry. Nondegenerate modes transform as the unit representation. Tracking these nondegenerate eigenvalues reveals a softening and also a mixing of modes as γ passes through γ_b.

Other studies consider more microscopic elastic network models [24,25] that place nodes at every C^α atom in the amino acid chains. These studies find that the displacements during maturation (i.e., as the virus goes through the buckling transition) can be accurately represented using a super-
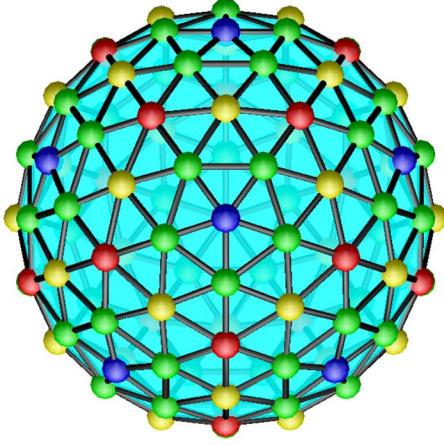
FIG. 1. (Color online) Triangulated network of $P=Q=2$. Colors identify local environments with fivefold vertices shown in blue.

FIG. 2. (Color online) Shell shape above the buckling transition for $P=128$, $Q=0$ shell with $k_s=1$ and $k_b=16$, yielding Foppl–von Karman number $\gamma=930$. Color coding is logarithmic according to total elastic energy (violet=low, red=high).

position of only the lowest few nondegenerate modes, consistent with our expectations. A normal-mode analysis of a full atomic model with reduced degrees of freedom [26] illustrates both symmetric and nonsymmetric modes and classifies these using group representations.

Section II of this paper reviews the continuum-elastic theory for deformations of planes and spheres, to establish notation and for comparison with our later numerical results. Our network model is defined in Sec. III and applied to the special cases of disclination-free triangular lattices, single disclinations of positive charge, and icosahedral structures of spherical topology containing 12 disclinations. Low-lying eigenvalue spectra reveal a sharp buckling transition in the case of a single disclination but a broadly smeared transition for the icosahedral case. Following Ref. [5], we find that the positive curvature of the sphere plays a symmetry-breaking role analogous to that of an applied magnetic field at a ferromagnetic phase transition.

The final section (Sec. IV) applies forces to selected points on a plane or a shell to probe the elastic response of the network as a whole. The resulting displacements define susceptibilities which diverge in the case of the single disclination. In the case of the icosahedron, we find that the effective stiffness (inverse of the susceptibility) drops most rapidly at γ_b for forces applied at fivefold symmetry axes, but the stiffness falls off more rapidly for forces applied at two- and threefold symmetry axes for $\gamma > \gamma_b$. We analyze these susceptibilities in the limiting cases of small and large γ.

II. CONTINUUM-ELASTIC THEORY

The general elasticity theory of membranes can be expressed in coordinate-free form [11,27]. Let M be a manifold (a two-dimensional smooth surface embedded in three-dimensional space) assumed to be in mechanical equilibrium. Now impose a tangential deformation $\mathbf{u}(\mathbf{x})$ and a normal deformation $\zeta(\mathbf{x})$ corresponding to displacements of points $\mathbf{x}$ on the surface. Let $g_{\alpha\beta}$ and $C_{\alpha\beta}$ be the metric and curvature tensors, respectively, of M after distortion. Greek indices take values 1 and 2 corresponding to the dimensions of M. Define the strain tensor
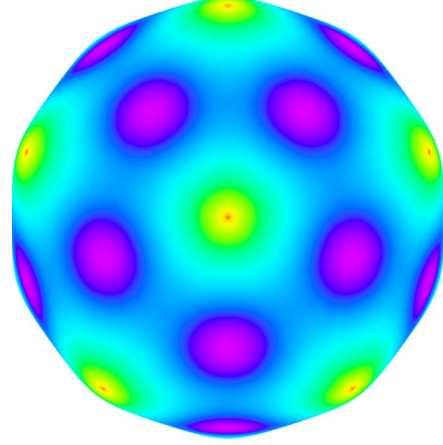
$$U_{\alpha\beta} = u_{\alpha\beta} + \zeta C_{\alpha\beta}, \tag{2}$$

where $u_{\alpha\beta} = \frac{1}{2}(D_\alpha u_\beta + D_\beta u_\alpha)$ and D_α indicates covariant differentiation with respect to x_α. The trace U_γ^γ measures dilation, while

$$S_{\alpha\beta} = U_{\alpha\beta} - \frac{1}{2} g_{\alpha\beta} U_\gamma^\gamma \tag{3}$$

measures shear strain. Bending of M is characterized by the mean curvature $H = \frac{1}{2} C_\gamma^\gamma$ and Gaussian curvature $K = \det C$.

The free energy density at $\mathbf{x}$ contains dilation, shear, and bending contributions,

$$f(\mathbf{x}) = f_d + f_s + f_b, \tag{4}$$

and can be integrated over M to obtain the total free energy

$$F = \int f(\mathbf{x}) \sqrt{\det g} \, d^2\mathbf{x}. \tag{5}$$

The separate contributions are

$$f_d(\mathbf{x}) = \frac{1}{2}(\lambda + \mu)(U_\gamma^\gamma)^2,$$

$$f_s(\mathbf{x}) = \mu S^{\alpha\beta} S_{\alpha\beta},$$

$$f_b(\mathbf{x}) = \frac{1}{2}\kappa(2H - c_0)^2 + \kappa_G K. \tag{6}$$

The elastic constants λ and μ are the Lamé constants [28]. The two-dimensional (2D) area (bulk) modulus $B = \lambda + \mu$, while μ itself is the shear modulus, and the 2D Young's modulus $Y = 4\mu(\lambda + \mu)/(\lambda + 2\mu)$. Upon integration over the surface M, the Gaussian curvature term becomes constant, and we neglect this term henceforth. Likewise, we set the spontaneous curvature $c_0 = 0$, thus assuming that the manifold M would be flat in the absence of constraints associated with the spherical topology. Effects of $c_0 \neq 0$ are discussed in Ref. [6].

Given the elastic free energy F, we obtain the stress tensor

$$\sigma^{\alpha\beta}(\mathbf{x}) = \frac{\delta F}{\delta U_{\alpha\beta}(\mathbf{x})}, \tag{7}$$

whose divergence yields the tangential force

$$F^{\beta} = D_{\alpha}\sigma^{\alpha\beta}. \tag{8}$$

The normal force is given by

$$N(\mathbf{x}) = -\frac{\delta F}{\delta \zeta(\mathbf{x})}. \tag{9}$$

In mechanical equilibrium, the stress tensor and normal force vanish. Slightly out of equilibrium, to first order in the displacements, special forms of $\mathbf{u}(\mathbf{x})$ and $\zeta(\mathbf{x})$ known as normal modes solve the eigenvalue equation

$$(\mathbf{F}, N) = -\Lambda(\mathbf{u}, \zeta). \tag{10}$$

When displaced from equilibrium according to the kth normal mode $(\mathbf{u}_k, \zeta_k)$, the free energy increases by

$$\Delta F = \frac{1}{2}\Lambda_k \int (|\mathbf{u}_k|^2 + \zeta_j^2) d\mathbf{x}. \tag{11}$$

According to the equipartition theorem, the modes fluctuate with thermal energy $\Delta F = k_B T/2$ and amplitude $\int(|\mathbf{u}_k|^2 + \zeta_k^2) d\mathbf{x} = 2k_B T/\Lambda_k$.

The time dependence of the strains depends on the equations of motion. In the overdamped case we write

$$\dot{u}^{\beta}(\mathbf{x}) = \Gamma F^{\beta}(\mathbf{x}), \quad \dot{\zeta}(\mathbf{x}) = \Gamma N(\mathbf{x}), \tag{12}$$

where we take Γ proportional to the inverse viscosity as in a Stokes-Einstein relation. In this case a normal mode decays in time with a decay rate $\omega = \Gamma \Lambda$. Reference [29] carries out a more thorough investigation of flat membranes coupled to fluid flow. In the absence of damping we write

$$\rho \ddot{u}^{\beta}(\mathbf{x}) = F^{\beta}(\mathbf{x}), \quad \rho \ddot{\zeta}(\mathbf{x}) = N(\mathbf{x}) \tag{13}$$

with ρ the 2D mass density. A normal mode now oscillates in time at frequency $\omega = \sqrt{\Lambda/\rho}$.

A. Deformations of a plane

An infinite flat elastic sheet in equilibrium has no curvature, so for small perturbations the energy decouples into contributions from the in-plane strain $\mathbf{u}$ and the perpendicular displacement ζ:

$$f = \frac{1}{2}\lambda(u_{\gamma}^{\gamma})^2 + \mu u^{\alpha\beta}u_{\alpha\beta} + \frac{1}{2}\kappa(\Delta\zeta)^2. \tag{14}$$

Here $\Delta = D_{\alpha}D^{\alpha} = \nabla^2$ is the usual 2D Laplacian operator and ∇ the usual gradient. By differentiating the energy we obtain the forces

$$\mathbf{F} = (\lambda + \mu)\nabla\nabla\cdot\mathbf{u} + \mu\Delta\mathbf{u} \tag{15}$$

and

$$N = -\kappa\Delta^2\zeta. \tag{16}$$

Because the in-plane and out-of-plane displacements decouple, we solve them separately. The solutions are based on the plane wave function

$$\psi_{\mathbf{k}}(\mathbf{r}) = e^{i\mathbf{k}\cdot\mathbf{r}}, \tag{17}$$

which is an eigenfunction of the Laplacian operator $\Delta\psi_{\mathbf{k}}(\mathbf{r}) = -k^2\psi_{\mathbf{k}}(\mathbf{r})$. In-plane normal modes are expressed as longitudinal waves

$$\mathbf{u}_L(\mathbf{r}) = \nabla\psi_{\mathbf{k}}(\mathbf{r}) = i\mathbf{k}e^{i\mathbf{k}\cdot\mathbf{r}} \tag{18}$$

and transverse waves

$$\mathbf{u}_T(\mathbf{r}) = \hat{z}\times\mathbf{u}_L = i(k_x\hat{y} - k_y\hat{x})e^{i\mathbf{k}\cdot\mathbf{r}}. \tag{19}$$

Note the identities $\nabla\times\mathbf{u}_L = 0$ and $\nabla\cdot\mathbf{u}_T = 0$, as expected for longitudinal and transverse waves. These waves are eigenvectors of the in-plane force Eq. (15) provided their eigenvalues obey the longitudinal and transverse dispersion relations, respectively,

$$\Lambda_L = (\lambda + 2\mu)k^2 \tag{20}$$

and

$$\Lambda_T = \mu k^2. \tag{21}$$

Perpendicular out-of-plane waves

$$\mathbf{u}_P(\mathbf{r}) = \hat{z}\psi_{\mathbf{k}}(\mathbf{r}) \tag{22}$$

obey Eq. (16) subject to the perpendicular wave dispersion relation

$$\Lambda_P = \kappa k^4. \tag{23}$$

For future reference, we recast the normal modes in plane-polar coordinates (r, ϕ), replacing the plane wave function $\psi_{\mathbf{k}}(\mathbf{r})$ with cylindrical Bessel functions

$$\psi_{km}(r, \phi) = J_m(kr)e^{im\phi}. \tag{24}$$

The Laplacian operator takes the form

$$\Delta = \frac{1}{r}\frac{\partial}{\partial r}\left(r\frac{\partial}{\partial r}\right) + \frac{1}{r^2}\frac{\partial^2}{\partial\phi^2}. \tag{25}$$

Like the plane wave function $\psi_{\mathbf{k}}(\mathbf{r})$, waves of type (24) are eigenfunctions of the Laplacian operator, $\Delta\psi_{km}(r, \phi) = -k^2\psi_{km}(r, \phi)$. Upon defining normal modes $\mathbf{u}_L$, $\mathbf{u}_T$, $\mathbf{u}_P$ as in Eqs. (18), (19), and (22) the longitudinal, transverse, and perpendicular dispersion relations given in Eqs. (20), (21), and (23) result. These polar forms generalize nicely to conical and spherical geometries.

B. Deformations of a sphere

Now we redo the prior calculation of Sec. II A for the case of small perturbations around a sphere of equilibrium radius R. In this case, the unperturbed manifold has constant mean curvature $H_0 = 1/R$. Consequently the free energy acquires a term coupling the in-plane and normal strains through the dilation energy,

$$f_d = \frac{1}{2}(\lambda + \mu)(u_{\gamma}^{\gamma} + 2\zeta/R)^2,$$

$$f_s = \mu[u_{\alpha\beta}u^{\alpha\beta} - (u_\gamma^\gamma)^2],$$

$$f_b\sqrt{\det g} = \frac{1}{2}\kappa\left[\left(\frac{2}{R} - \Delta\zeta\right)^2 - \frac{2}{R^2}(D_\alpha\zeta)^2\right]. \qquad (26)$$

In the above, the Laplacian operator takes the form

$$\Delta = \frac{1}{R^2\sin\theta}\frac{\partial}{\partial\theta}\left(\sin\theta\frac{\partial}{\partial\theta}\right) + \frac{1}{R^2\sin^2\theta}\frac{\partial^2}{\partial\phi^2}. \qquad (27)$$

Notice that we include the integration measure $\sqrt{\det g}$ along with the bending energy f_b, because it contributes the term $(D_\alpha\zeta)^2$. The $\sqrt{\det g}$ factor is not needed in f_d or f_s because these are already second order in the deformation.

Taking functional derivatives of F yields the stress tensor and in-plane and normal forces

$$\sigma^{\alpha\beta} = \lambda g^{\alpha\beta}\left(u_\gamma^\gamma + \frac{2}{R}\zeta\right) + 2\mu\left(u^{\alpha\beta} + \frac{1}{R}g^{\alpha\beta}\zeta\right),$$

$$F^\beta = (\lambda + \mu)D^\beta\left(u_\gamma^\gamma + \frac{2}{R}\zeta\right) + \mu\left(\Delta + \frac{1}{R^2}\right)u^\beta,$$

$$N = -(\lambda + \mu)\left(\frac{2}{R}u_\gamma^\gamma + \frac{4}{R^2}\zeta\right) - \kappa\mathcal{L}\zeta, \qquad (28)$$

where we define

$$\mathcal{L} = D_\alpha D^\alpha D_\beta D^\beta + \frac{2}{R^2}D_\alpha D^\alpha. \qquad (29)$$

The extra $\mu u^\beta/R^2$ in Eq. (28) for F^β comes from commutation of covariant derivatives. The final, second-derivative, term in (29) comes from integrating by parts the square of the first derivative in $f_b\sqrt{\det g}$.

Take the spherical harmonic $Y_{lm}(\theta, \phi)$ as the basic deformation, analogous to the plane wave $e^{i\mathbf{k}\cdot\mathbf{r}}$ in Eq. (17) or the cylindrical wave $J_m(kr)e^{im\phi}$ in Eq. (24). The spherical harmonic is an eigenfunction of Δ with eigenvalue $-l(l+1)/R^2$ and an eigenfunction of $\mathcal{L}$ with eigenvalue $l(l-1)(l+1)(l+2)/R^4$. By analogy with the procedure for plane waves in flat space, we take derivatives as

$$\mathbf{u}_L = R\,\nabla\,Y_{lm}, \quad u_L^\alpha = RD^\alpha Y_{lm},$$

$$\mathbf{u}_T = \hat{\mathbf{r}}\times\mathbf{u}_L, \quad u_T^\alpha = R\epsilon_\beta^\alpha D^\beta Y_{lm}, \qquad (30)$$

where ϵ is the alternating tensor. We also define

$$\mathbf{u}_P = \hat{\mathbf{r}}Y_{lm}. \qquad (31)$$

These functions are linear combinations of the "vector spherical harmonics" $\mathbf{V}_{lm}$, $\mathbf{W}_{lm}$, and $\mathbf{X}_{lm}$, which form a complete set of orthogonal functions for expanding vector fields on the surface of a sphere [23,30]. Notice that the transverse mode $\mathbf{u}_T$ is proportional to the angular momentum operator acting on Y_{lm}, thus identifying it with the vector spherical harmonic $\mathbf{X}_{lm}$. The longitudinal and perpendicular modes $\mathbf{u}_L$ and $\mathbf{u}_P$ are linear combinations of $\mathbf{V}_{lm}$ and $\mathbf{W}_{lm}$. Note that the longitudinal and transverse modes $\mathbf{u}_L$ and $\mathbf{u}_T$ exist only for $l \geq 1$, while $\mathbf{u}_P$ exists for $l \geq 0$.

The transverse mode $\mathbf{u}_T$ is divergenceless ($u_\gamma^\gamma = 0$) and hence creates no perpendicular force N and no longitudinal force (the gradient part of F^β). In fact, it is an eigenfunction of the force (28). Upon taking into account the commutation of covariant derivatives, we find $F^\beta = [\mu(l-1)(l+2)/R^2]u_T^\beta$, from which we obtain the eigenvalue

$$\Lambda_T = \mu\frac{(l-1)(l+2)}{R^2}. \qquad (32)$$

As expected, $\Lambda_T = 0$ for $l = 1$ because these modes correspond to rigid rotations.

In contrast to the transverse modes, the longitudinal and perpendicular modes $\mathbf{u}_L$ and $\mathbf{u}_P$ are coupled in both the tangential force F^β and perpendicular force N. In matrix form,

$$\begin{pmatrix} F^\alpha \\ N \end{pmatrix} = \begin{pmatrix} M_{LL} & M_{LP} \\ M_{PL} & M_{PP} \end{pmatrix}\begin{pmatrix} u_L^\alpha \\ \zeta \end{pmatrix}. \qquad (33)$$

Setting $\mathbf{u}_L$ as in Eq. (30) and setting ζ as the radial component of $\mathbf{u}_P$ in Eq. (31), the matrix elements of M become

$$M_{LL} = (\lambda + \mu)\frac{l(l+1)}{R^2} + \mu\frac{(l-1)(l+2)}{R^2},$$

$$M_{LP} = (\lambda + \mu)\frac{2}{R^2},$$

$$M_{PL} = (\lambda + \mu)\frac{2l(l+1)}{R^2},$$

$$M_{PP} = (\lambda + \mu)\frac{4}{R^2} + \kappa\frac{(l-1)l(l+1)(l+2)}{R^4}. \qquad (34)$$

The eigenvalues of this matrix, $\lambda_\pm$, are the desired normal-mode eigenvalues Λ. For the special case $l = 1$, the eigenvalues are $\lambda_- = 0$ and $\lambda_+ = 6(\lambda + \mu)/R^2$. The vanishing eigenvalue λ_- corresponds to rigid translation (for example, the north and south poles displace upward perpendicular to the shell while the equator displaces upward tangent to the shell). The finite eigenvalue λ_+ corresponds to an "optical" mode in which polar and equatorial regions displace in opposite directions (for example, the north and south poles displace upward while the equator displaces downward).

The spherical solution should go smoothly to the flat space solution in polar coordinates as the sphere radius $R \to \infty$. This correspondence can be verified by holding $r = R\theta$, $k = l/R$, and m fixed, and noting that [31]

$$\lim_{l\to\infty}\sqrt{\frac{4\pi}{2l+1}}Y_{lm}(\theta, \phi) = (-1)^m J_m(kr)e^{im\phi}. \qquad (35)$$

In addition, the eigenvalues should approach their proper limits. Clearly, Λ_T approaches its flat space limit (21). To check $\Lambda_{L,P}$, note that the eigenvalues $\lambda_\pm$ of the matrix (34) approach $(\lambda + 2\mu)l(l+1)/R^2$ and $\kappa(l-1)l(l+1)(l+2)/R^4$ in the limit of large sphere radius R, yielding the flat space limits Eqs. (20) and (23).

III. MASS-AND-SPRING MODEL

We now introduce the discrete mass-and-spring model for which numerical calculations will be performed. This model is also closer to reality for liposomes and colloidosomes, which consist, respectively, of discrete lipid molecules and colloidal particles, and also for viruses, which consist of an aggregation of discrete protein subunits known as capsomers. Let $\mathbf{r}_i$ be the position of mass i and $\hat{\mathbf{n}}_I$ be the orientation of plaquette I. A plaquette is a set of three masses joined to each other by springs, and we take the normal in the outward direction. Following [5], we define

$$\mathcal{H}_s = \frac{k_s}{2} \sum_{\langle ij \rangle} (|\mathbf{r}_i - \mathbf{r}_j| - a)^2 \qquad (36)$$

and

$$\mathcal{H}_b = \frac{k_b}{2} \sum_{\langle IJ \rangle} |\hat{\mathbf{n}}_I - \hat{\mathbf{n}}_J|^2 \qquad (37)$$

and set the unstretched spring length $a=1$. Here $\langle ij \rangle$ denote pairs of nearest-neighbor vertices, and $\langle IJ \rangle$ denote pairs of adjacent (edge-sharing) plaquettes. In the continuum limit the discrete model reproduces the continuum system with elastic constants

$$Y = \frac{2}{\sqrt{3}} k_s, \qquad \kappa = \frac{\sqrt{3}}{2} k_b, \qquad (38)$$

Foppl–von Karman number

$$\gamma = \frac{Y R^2}{\kappa} = \frac{4 k_s R^2}{3 k_b}, \qquad (39)$$

Lamé coefficients and bulk modulus

$$\lambda = \mu = \frac{\sqrt{3}}{4} k_s, \qquad B = \frac{\sqrt{3}}{2} k_s, \qquad (40)$$

and 2D mass density (taking the vertex mass $m=1$)

$$\rho = 2/\sqrt{3}. \qquad (41)$$

A. Deformations from flat space

Consider a regular six-coordinated triangulated network of masses and springs. As before we start with the plane wave function (17) and take its gradient to obtain the longitudinal sound wave. The dispersion relation is simplest for wave vector $\mathbf{k}$ in the $\hat{y}$ direction (chosen to lie midway between two near-neighbor bonds),

$$\Lambda_L = 3 k_s \left[1 - \cos\left(\frac{\sqrt{3}}{2} k_y a \right) \right]. \qquad (42)$$

Taking the cross product with $\hat{z}$ yields the transverse sound wave with dispersion relation

$$\Lambda_T = k_s \left[1 - \cos\left(\frac{\sqrt{3}}{2} k_y a \right) \right]. \qquad (43)$$

Finally, taking the perpendicular displacements as the plane wave yields the perpendicular modes with dispersion relation
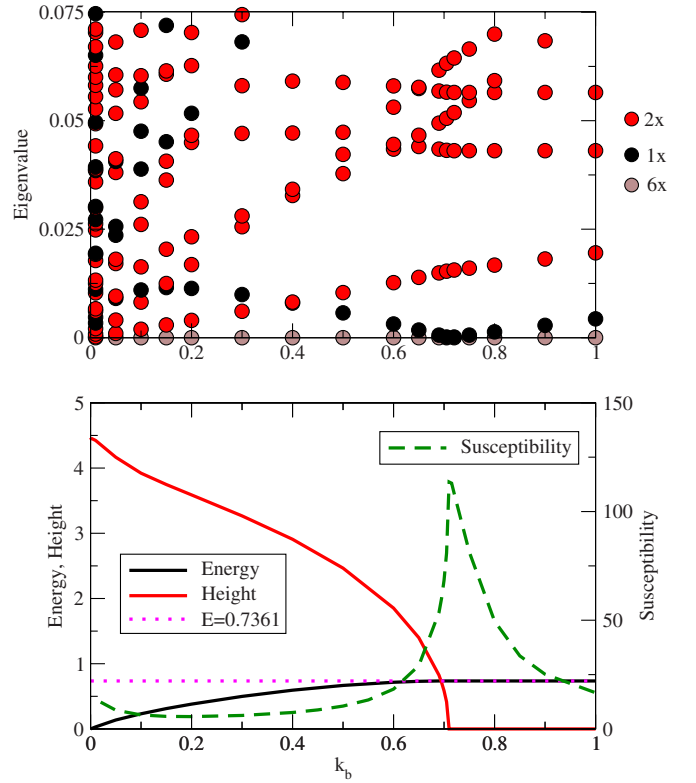

FIG. 3. (Color online) Triangulated network of radius $8a$ and spring constant $k_s=1$ with a single fivefold disclination at center. (Top) Eigenvalue spectrum color coded according to degeneracy. Note the nondegenerate $1X$ mode that goes to zero at the buckling transition. (Bottom) Energy, cone height, and susceptibility.

$$\Lambda_P = k_b \left[2 - 2 \cos\left(\frac{\sqrt{3}}{2} k_y a \right) \right]^2. \qquad (44)$$

In the continuum limit $ka \ll 1$, these dispersion relations revert to the prior results of continuum-elastic theory.

B. Buckling of a plane into a cone

Upon introducing a fivefold $+2\pi/6$ disclination into the flat triangulated network discussed previously, strain energy accumulates [12] and grows without bound as the radius R of the network increases. At some specific "buckling radius" R_b it becomes energetically favorable to buckle out of plane, trading a reduction in strain energy for a cost in bending energy. The trade-off is measured by the Foppl–von Karman number γ. Small γ favors flat networks, while larger γ favors buckling into a conical shape.

In the following, we analyze the vibrational spectrum of the network as it passes from flat to conical. Rather than vary the radius, we hold R fixed and vary the bending stiffness. Large k_b opposes buckling and the network lies flat, while small k_b allows buckling out of plane into a cone. For the network of radius $R=8a$ analyzed below, buckling occurs for $k_b \approx 0.71$. As R increases the threshold value of k_b grows as R^2, so that γ approaches the limiting value $\gamma_b \approx 154$ [5,12].

Eigenvectors of the Hessian matrix form basis functions for representations of the symmetry group of the structure

TABLE I. Character table of C_{5v}. C_n denotes conjugacy class of order n. Values of m denote in-plane angular momenta. $\tau=(\sqrt{5}+1)/2$ is the golden mean.

C_{5v}	m	$1C_0$	$2C_5$	$2C_5^2$	$5\sigma_v$
A_1	0	1	1	1	1
A_2	0	1	1	1	-1
E_1	1	2	τ^{-1}	$-\tau$	0
E_2	2	2	$-\tau$	τ^{-1}	0

[32]. Eigenvectors sharing a common eigenvalue form the basis for an irreducible representation. Thus the patterns of degeneracy follow the dimensionalities of the irreducible representations, as can be seen in Fig. 3(a). Likewise, the eigenvectors exhibit special symmetry properties associated with subgroups of the full symmetry group.

The symmetry point group of the cone is C_{5v} in general, corresponding to fivefold rotations around an axis passing through the five-coordinated vertex, together with reflections in vertical planes passing through this axis (see Table I). For the specific case of the flat network, the group is even higher, D_{5h}, adding reflections in the horizontal plane, and twofold rotations around axes lying within the plane. For both groups all irreducible representations are either one or two dimensional, so all nonzero eigenvalues must be nondegenerate or twofold degenerate. Of course, there must be a sixfold degeneracy of zero eigenvalues, corresponding to rigid translations and continuous rotations (not belonging to the finite point group) that leave the energy invariant.

For the group D_{5h}, the irreducible representations are based on those of C_{5v} supplemented with an additional label g, u according to whether they are even (g) or odd (u) under reflection through the horizontal plane σ_h. The requirement that each irreducible representation be either even or odd under σ_h requires that each mode be polarized either fully in plane or fully perpendicular.

Let Λ_1 be the lowest nonzero eigenvalue. Its eigenvector $\mathbf{e}_1$ is polarized strictly perpendicular to the sheet and transforms as the irreducible representation A_{2u}. Its value is nonzero at the origin. The energy of mode i varies as $\Lambda_i a_i^2$ where a_i measures the amplitude of the mode. Mechanical equilibrium thus demands that all eigenvalues (other than the six zero modes) be strictly positive. In particular, it requires $\Lambda_1>0$. However, if we monitor the value of Λ_1 as a function of γ [Fig. 3(a)] we find it crosses through zero at γ_b.

For small deformations we express the energy as

$$E = \sum_i \frac{1}{2}\Lambda_i a_i^2 + O(a_i^4). \tag{45}$$

Now set $\Lambda_1=c(\gamma_b-\gamma)$. The mechanically stable minimum energy structure is perfectly flat ($a_i=0$) for $\gamma<\gamma_b$, but it buckles out of plane for $\gamma>\gamma_b$, in a shape described by the eigenvector $\mathbf{e}_1$, with amplitude growing as $\sqrt{\gamma-\gamma_b}$. Meanwhile, the energy drops as $(\gamma-\gamma_b)^2$. These effects can be seen in Fig. 3(b).

For $\gamma>\gamma_b$, Fig. 3(a) shows the spectrum of vibrations around the mechanically stable, buckled structure. Note that Λ_1' (the lowest nondegenerate eigenvalue) becomes positive again.

C. Buckling of spherical shells

1. $P=1$, $Q=0$ icosahedron

Table II presents the character table of the 60-element icosahedral rotational symmetry group Y, which has five irreducible representations. The conjugacy classes are labeled C_n, where n is the order of elements in the class, so that an element of C_n corresponds to a rotation by $2\pi/n$. Recall that the spherical harmonics Y_{lm} form basis functions for the irreducible representations of the continuous rotation group SO(3), and therefore they induce representations (in general reducible) of Y. For a given angular momentum l and rotation angle θ, the character is

TABLE II. Character table of Y. C_n denotes conjugacy class of order n. Values of l denote angular momenta. R is the regular representation and V the total vibrational representation discussed in Sec. III C 1.

Y	l	$1C_0$	$15C_2$	$20C_3$	$12C_5$	$12C_5^2$
A	0	1	1	1	1	1
F_1	1	3	-1	0	τ	$-\tau^{-1}$
F_2	(3)	3	-1	0	$-\tau^{-1}$	τ
G	(3)	4	0	1	-1	-1
H	2	5	1	-1	0	0
R		12	0	0	2	2
V		36	0	0	2τ	$-2\tau^{-1}$

TABLE III. Vibrational eigenvalues for $P=1$, $Q=0$ icosahedron with $a=k_s=1$, $k_b=0$. Λ is the eigenvalue and g the degeneracy. $R=\sqrt{1+\tau^2}/2=0.951\,06$ is the radius of the icosahedron.

Λ	Formula	Irrep	g	Comments
0.00000	0	$2\times F_1$	6	Translations+rotations
0.58579	$2-\sqrt{3}$	H_a	5	Mixed, contains $\mathbf{V}_{2m}$ and $\mathbf{W}_{2m}$
0.76393	$\sqrt{5}/R^2-2$	F_2	3	Radial, contains $\mathbf{r}Y_{3m}$
1.00000	1	H	5	Tangent $\mathbf{X}_{2m}$
1.80901	$1+\tau/2$	G_a	4	Tangent $\mathbf{X}_{3m}$
2.76393	$\sqrt{5}/R^2$	A	1	Radial $\mathbf{r}Y_{00}$ breathing mode
3.00000	3	F_1	3	Mixed $\mathbf{V}_{1m}$
3.41421	$2+\sqrt{2}$	H_b	5	Mixed
3.42705	$1+3\tau/2$	G_b	4	Tangent

$$\chi_l(\theta) = \frac{\sin(l+1/2)\theta}{\sin\theta/2}. \tag{46}$$

Irreducible representations (irreps) of Y are labeled in Table II according to the lowest angular momentum l under which they transform. Of particular interest is the representation F_1 corresponding to angular momentum $l=1$. This is the representation under which three-dimensional vectors transform.

The simple icosahedron has 12 vertices, 20 faces, and 30 edges. Since we place masses on the vertices, our eigenstates are functions defined only at vertex positions. Arbitrary scalar-valued functions can be expressed as linear combinations of the basis functions of the "regular representation," one of which is concentrated at each icosahedron vertex. The characters χ_R of the regular representation equal the number of vertices that remain stationary under a given symmetry operation. Our vibrational modes are *vector-valued* functions on the set of vertices and thus can be expressed as linear combinations of the product of the regular representation R times the representation F_1 corresponding to a three-dimensional vector. We call the resulting product representation the "total vibrational representation" [23], and its characters $\chi_V = \chi_R \chi_{F_1}$.

Reducible representations can be decomposed into their irreducible components using orthogonality properties of character tables. In particular we obtain the decomposition

$$V = A \oplus 3F_1 \oplus F_2 \oplus 2G \oplus 3H. \tag{47}$$

Of the three occurrences of the vector representation F_1, we know that two must correspond to rigid global translations and rotations. These leave the energy invariant and hence are zero-frequency modes. The nondegenerate mode transforming as the unit representation A must correspond to a "breathing mode" in which all vertices displace equally in the radial direction. We find that the remaining modes have specific interpretations in terms of vector spherical harmonics, as listed in Table III.

2. Higher-order icosahedra

As the icosahedron is subdivided and the total number of vertices grows, the classification of modes into irreducible
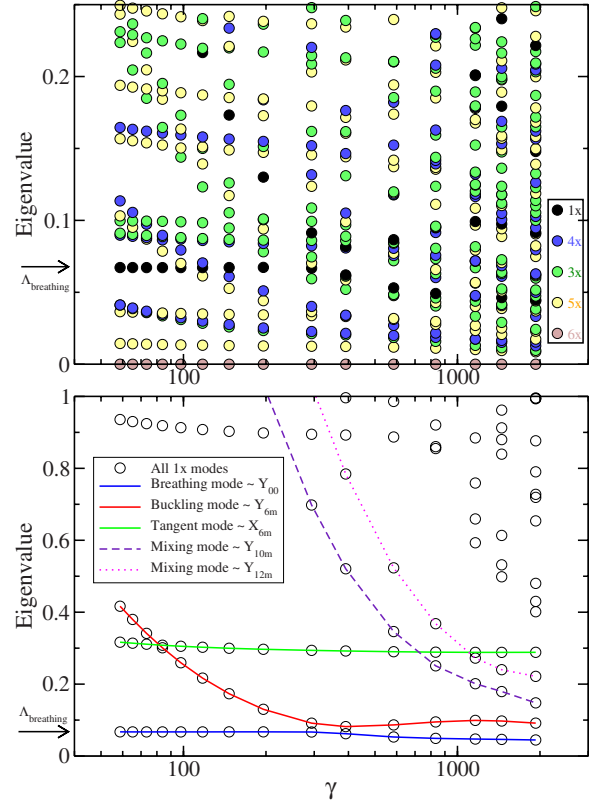

FIG. 4. (Color online) Lowest-frequency modes of $P=8$, $Q=0$ icosahedron with $N_v=642$ vertices: (top) color coded according to degeneracy; (bottom) nondegenerate modes only. Arrows locate eigenvalue $\Lambda_{breathing}=8\pi\sqrt{3}/N_v$. Note that the buckling mode (red) dips close to zero near the buckling transition.

representations remains similar, but each irreducible representation now occurs many times. Figure 4(a) shows the lowest-frequency modes for a $P=8$, $Q=0$ icosahedron with $N_v=642$ vertices. To obtain this figure, we set $k_s=1$, and varied k_b. For each value of k_b we relaxed the structure to mechanical equilibrium using steepest descents, evaluated the Hessian matrix by numerical differentiation, and then diagonalized the matrix. The Foppl–von Karman number is defined as in Eq. (39), where now R is defined as the root-mean-square radius[1] and takes values in the range 6.6–7.6 for the $P=8$, $Q=0$ icosahedron.

Owing to the rotation and translation invariance of the total energy, we always have a sixfold degenerate mode of zero eigenvalue. The remaining eigenvalues fall into the classification of icosahedral symmetry introduced in Table II.

At low γ, when the shape is spherical in the continuum limit of large radius, and the energy cost of bending dominates over the energy cost of stretching or shearing, the lowest-frequency nondegenerate mode is a breathing mode, corresponding to a sphere with oscillating radius. Perturbing the radius by an amount ζ (i.e., adding mode $\mathbf{u}_P=\hat{\mathbf{r}}\zeta$) increases the energy by $8\pi B\zeta^2$ while displacing N_v vertices by

---

[1]Defining R instead as the mean radius [5] has little impact below or near the buckling transition and results only in a slight rescaling as γ grows large.
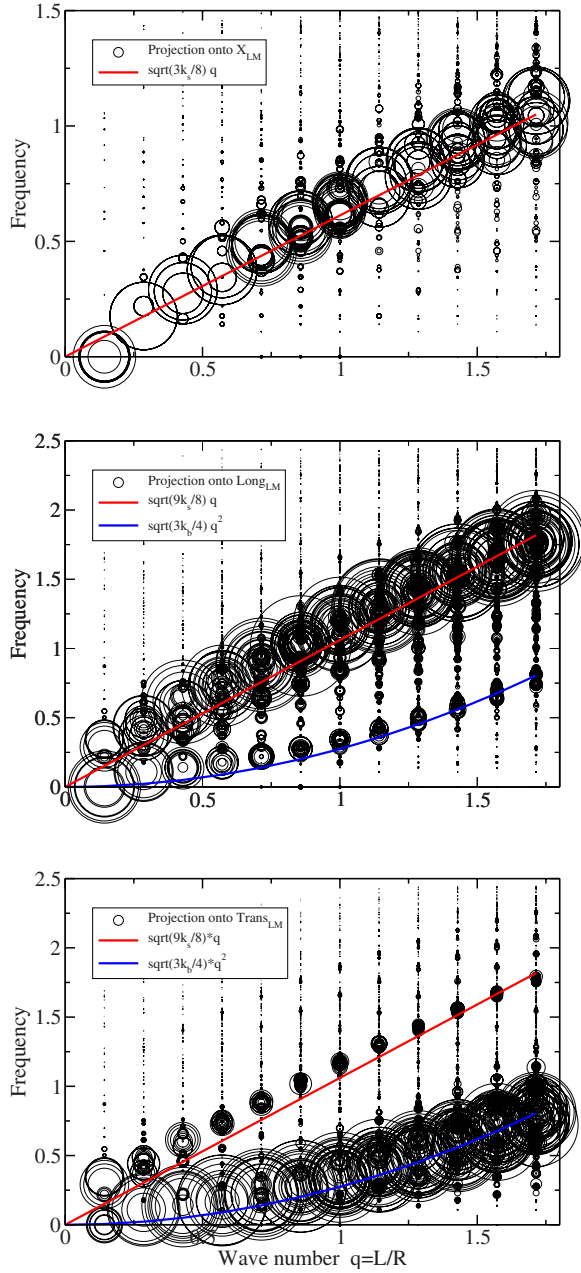
FIG. 5. (Color online) Vibrational frequencies plotted versus wave number $q = l/R$, where l is the angular momentum index. Data are for $P=8$, $Q=0$ icosahedron with $k_s=1$, $k_b=0.1$, $\gamma=653$. The radii of the circles indicate the sizes of the various projections.

ζ. Identifying the energy with $\frac{1}{2}N_v\Lambda_{breathing}$, and noting the area modulus $B=\sqrt{3}/2$, we find the eigenvalue $\Lambda_{breathing}=8\pi\sqrt{3}k_s/N_v$, which fits well to the data in Fig. 4.

At higher frequencies, where the wavelength of the modes becomes small compared to the radius of curvature, we expect that the eigenvalues should revert to their flat space limits as discussed in Sec. II B. The validity of this hypothesis is demonstrated in the dispersion relations shown in Fig. 5. Here we plot the vibrational frequencies (i.e., the square roots of Hessian eigenvalues) as functions of the equivalent wave number, defined as the angular momentum index l divided by the radius R. The radii of the circles represent the

projections of the eigenvectors onto the vector spherical harmonics $\mathbf{X}_{lm}$ (top), and the longitudinal and transverse eigenfunctions $\mathbf{u}_L$ and $\mathbf{u}_T$ (middle and bottom). The solid lines are the predictions of continuum elastic theory for the plane, Eqs. (20)–(22).

Soft-mode behavior at the buckling transition is less pronounced than in the case of the cone. The crossover from spherical to faceted shape, which occurs gradually for $\gamma \sim 100$–1000, preserves the icosahedral symmetry. As such, the displacements respect icosahedral symmetry. If the transition is due to a soft mode, this mode itself must be invariant under operations of the icosahedral symmetry group. That is, it must transform as the unit representation and therefore must be nondegenerate. The soft mode is best seen in Fig. 4(b), where only the nondegenerate modes are shown. Always the lowest-frequency nondegenerate mode is an $l=m=0$ breathing mode, and as just discussed its frequency does not depend significantly on k_b. However, the next occurrence of the unit representation, at $l=6$, contains a mode, of type $\mathbf{u}_P$ and labeled Y_{6m}, that does indeed soften and mixes with the breathing mode in an avoided crossing around $\gamma \approx 400$. Another $l=6$ mode, of type $\mathbf{u}_T$ and labeled $\mathbf{X}_{2m}$, is prevented by symmetry from mixing with the $\mathbf{u}_P$ mode. A series of other nondegenerate modes ($l=10,12,20,\ldots$) soften at higher γ values and mix with the other soft modes.

Around γ_b, the buckling mode consists predominantly of $l=0$ and 6 spherical harmonics, with a small admixture of $l=10$ and higher harmonics. The weight of this mode is concentrated in the vicinities of the icosahedron vertices, and it has strong overlap with the displacements of vertices under the buckling transition.

The forbidden crossing of the buckling and breathing mode smears the buckling transition, because $\Lambda_{buckling} > \Lambda_{breathing} > 0$ prevents the eigenvalue of the buckling mode from actually crossing zero. This contrasts with the case of the disclinated flat sheet buckling into a cone, where the eigenvalue does indeed cross zero. For the sheet-to-cone transition, the analog of the breathing mode is just a zero-energy translation, rather than a finite-frequency radial displacement. Also, up-down symmetry of the plane allows the crossing of the buckling mode (which is odd) with this translation. On a sphere, the symmetry breaking between inside and outside the sphere causes the breathing mode to mix with the buckling.

Owing to the smearing, the value of γ_b is not uniquely defined for the sphere-to-icosahedron transition. Reported values range from 130 to 260 based on fitted energy models [5,6]. We observe the avoided crossing around $\gamma \approx 400$.

IV. SUSCEPTIBILITIES

A. Cones

The soft-mode transition is a genuine sharp phase transition for the buckling of a disclinated sheet into a cone. We already discussed the order parameter (height) and energy variation through the transition, in Sec. III B. Now we consider the susceptibility, namely, the response of the order parameter to an applied field. In this case, we examine the

response of the buckling height to a point force applied at the disclination.

Assume the height of the cone (i.e., the vertical displacement of the five-coordinated particle at the center) is given by $h = \Sigma_i P_i a_i$, where again a_i is the amplitude and measures the projection of the mode i onto the height variable. Then in the presence of an applied force we express the energy as

$$E = \sum_i \left(\frac{1}{2} \Lambda_i a_i^2 - F P_i a_i \right), \tag{48}$$

which differs from (45) by the work done against the applied force. Minimizing the energy yields $a_i = F P_i / \Lambda_i$ resulting in total height $h = F \Sigma_i P_i^2 / \Lambda_i$ and susceptibility

$$\chi = \frac{\partial h}{\partial F} = \sum_i \frac{P_i^2}{\Lambda_i}. \tag{49}$$

Thus a vanishing eigenvalue, say Λ_1, passing linearly through zero at $\gamma = \gamma_b$, translates immediately into a diverging susceptibility. This divergence is evident in Fig. 3(b). Note that the amplitudes differ on the two sides of γ_b because in one case we perturb around a flat network while in the other we perturb around a buckled cone.

B. Spheres

Now consider the analogous response for the case of icosahedrally symmetric triangulated spheres and faceted icosahedra. We consider the inverse of the susceptibility as an effective spring constant $K = 1/\chi$, and make the spring constant dimensionless by dividing by the Young's modulus Y. We first present numerical results for symmetric forces over a wide range of γ values; then in later sections we consider the limiting cases of small and large γ. A similar analysis was carried out previously [33] using a slightly different form of curvature energy.

Our data were generated from a sequence of icosahedra of varying sizes and elastic properties. We consider nonchiral icosahedra with $P = Q$ ranging from 4 to 512 (i.e., N_v ranging from 482 to 7 864 322). To speed calculation, the full 120-element icosahedral symmetry group Y_h was employed, resulting in a speedup of nearly 120 times. Beyond the buckling transition the five-coordinated vertices sharpen, with a radius of curvature R_v related to the buckling radius

$$R_b = \sqrt{\gamma_b \kappa / Y} \approx 12.4 \sqrt{\kappa / Y} \tag{50}$$

by a geometrical factor of order 1. In order to approximate the continuum limit we chose to hold $k_s = 1$ fixed and keep $k_b \geq 1/2$, resulting in $R_b \geq 7.6a$.

Each structure was relaxed using the conjugate-gradient method. We found that the necessary number of relaxation steps diverges with increasing size, consistent with the $1/R^4$ vanishing relaxation rate predicted by Eq. (23). To ensure sufficient accuracy in the susceptibility, we used 128-bit real arithmetic in the final stages of all relaxations. For $P = Q = 512$, complete relaxation requires approximately two months on a 3.0 GHz Intel Xeon computer. For studies such as ours, which seek the continuum limit, a finite-element aproach [15,19,20] might be more computationally efficient than our discrete mass-and-spring model.
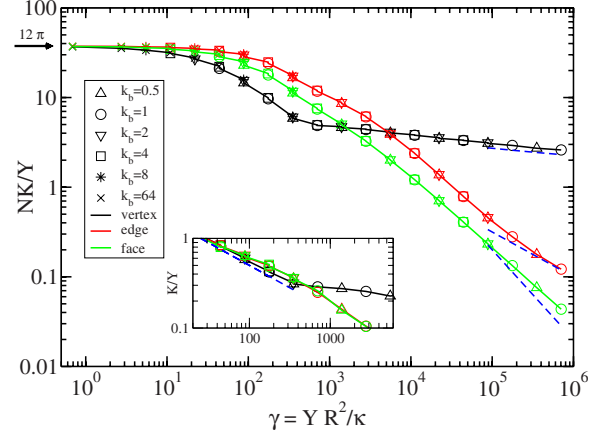

FIG. 6. (Color online) Stiffness (inverse susceptibility) to forces applied with icosahedral symmetry at vertices, edges, and faces. Dashed blue lines show $15/\ln(0.79\sqrt{\gamma})$ (vertex, offset from the best fit for clarity), $100/\sqrt{\gamma}$ (edge, scaling expected for $\gamma > 10^6$), and $20\,000/\gamma$ (face, scaling for bending of flat facet [9]). Inset: Diametrically opposed forces applied with uniaxial symmetry. Dashed blue line shows $5/\sqrt{\gamma}$.

Once the structure was relaxed without applied stress, we re-relaxed with a radially inward force F applied symmetrically at all $N = 12$ vertices, all $N = 20$ faces or all $N = 30$ edges. The effective spring constant $K = F/\zeta$ was defined as the applied force F divided by the displacement ζ of the mass to which the force was applied. We actually consider NK/Y because we define K as the derivative of ζ with respect to all N simultaneous applied forces F. A small applied force $F = 0.001$ was required to achieve linear response in cases where K became small.

Figure 6 shows numerical data for symmetric forces applied to vertices, edges, or faces. In the limit of small γ the three data sets converge to a γ-independent value. As γ increases, the vertices weaken more quickly than the faces or edges, consistent with our picture of the buckling transition as concentrating at the disclinations, which are located at vertices. However, beyond γ_b the vertex stiffness falls off very slowly, while both face and edge stiffness continue their rapid decline.

1. Small-γ limit

The following discussion first considers the limit of small γ, in which the shapes are nearly spherical and calculations can be done exactly. The response depends on whether the stress is applied in a uniaxial manner (e.g., at diametrically opposed points) or in a more symmetric manner (e.g., simultaneously at all vertices or faces, or edges, or even an isotropic pressure).

For an applied pressure P, the deformation is purely radial, with amplitude ζ as in the breathing mode discussed previously. This increases the energy by $8\pi B \zeta^2$, while doing work $4\pi R^2 P \zeta$ against the pressure. Balancing the two yields $\zeta = R^2 P / 4B$, susceptibility $\chi = \partial \zeta / \partial P = R^2 / 4B$, and spring constant $K/Y = 4B/YR^2$. In the case of N symmetrically applied point forces, we identify $P = NF/4\pi R^2$, yielding $NK/Y = 16\pi B/Y = 12\pi = 37.7$, where we used Eqs. (38) and (40).

The stiffness is independent of γ, consistent with the numerical result shown.

For uniaxial stress, let the displacement at the two poles be ζ and assume this displacement persists over a polar region of size d (see Sec. 15 of Ref. [28]). The bending energy density $f_b \sim \kappa(\zeta/d^2)^2$, and integrating over the polar region yields total bending energy $E_b = \kappa\zeta^2/d^2$. Meanwhile, the strain tensor $u_{\alpha\beta} \sim \zeta/R$ yields a total stretching energy [see Eq. (28)] $E_s \sim Y(\zeta/R)^2 d^2$. Minimizing the sum $E_s + E_b$ to find the optimal shape yields $d^4 \sim (\kappa/Y)R^2$ and $E_s + E_b \sim \sqrt{\kappa Y}\zeta^2/R$. Equating this to $F\zeta$, the work done against the applied force, we find $\zeta \sim (R/\sqrt{\kappa Y})F$ and $\chi = R/\sqrt{\kappa Y}$. The elastic constant $K/Y \sim 1/\sqrt{\gamma}$, independent of the axis along which the force is applied, consistent with our numerical results (see Fig. 6, inset).

2. Large-γ limit

For $\gamma > \gamma_b$, the radius of curvature at the icosahedron vertices quickly approaches R_v [Eq. (50)] and remains fixed independent of the icosahedron radius R. Forces applied at icosahedron vertices get transferred through the curved vertex region to the flat facets in a primarily longitudinal manner. According to the theory of longitudinal deformation of plates (see Sec. 13 of Ref. [28]), the displacement at large distances r from the applied force varies as $u(r) \sim (F/Y)\ln r/r_0$ with r_0 some fixed length. Upon setting $K = F/u(R)$ and choosing r_0 proportional to R_v, we find that $K/Y \sim c/\ln(b\sqrt{\gamma})$. The numerical data shown in Fig. 6 fit well to this form with values $c = 17.3$ and $b = 0.79$. The curve shown for comparison illustrates $c = 15$, imposing a uniform displacement for visual clarity.

For forces applied to the icosahedron edges we expect to see the onset of ridge-scaling behavior [17–22] as γ approaches 10^6. Unfortunately, the diverging relaxation time prevents us from exploring larger γ within our current calculational method, preventing us from observing this behavior cleanly. We briefly review the predictions of ridge scaling.

Let L (which is proportional to R) be the length of an icosahedron edge. At each end of this edge the facets join at a fixed angle of $\theta = 138.2°$. At the middle the edge sags inward by an amount ζ, creating a saddle-shaped ridge with a small radius of curvature R_1 across the ridge and a large (and negative) radius of curvature R_2 along the ridge [17]. The strain along the ridge line is of order $(\zeta/L)^2$. Because the facets on either side of the ridge approach the angle θ, the radius R_1 is proportional to the sag ζ [17]. Assuming that the bending and strain energy persist along the length L of the ridge and extend a distance R_1 to either side, we estimate the energy as

$$E = R_1 L[Y(\zeta/L)^4 + \kappa(1/R_1)^2] - F\zeta, \quad (51)$$

where the final term represents the action of a force F acting at mid-edge.

Upon setting $\zeta \sim R_1$ and varying R_1 to minimize the energy, we find, in the absence of force F,

$$R_1 \sim (\kappa/Y)^{1/6}L^{2/3} \sim \sqrt{\kappa/Y}\gamma^{1/3} \sim L\gamma^{-1/6}. \quad (52)$$

In the presence of a weak applied force F, the small radius R_1 increases by an amount of order

$$\Delta R_1 \sim \frac{L}{\sqrt{\kappa Y}}F. \quad (53)$$

Recalling that $\zeta \sim R_1$ and converting this to an effective spring constant $K = dF/d\zeta$ yields $K/Y \sim \sqrt{\kappa/YL^2} \sim 1/\sqrt{\gamma}$. Indeed, the edge elasticity in Fig. 6 seems to show a crossover toward slope $-1/2$ on our log-log plot.

Meanwhile, the icosahedron faces become almost planar in the limit of large γ. Timoshenko [9] discusses the deflection of an equilateral triangular plate under a load applied at the center. The deflection is proportional to R^2/κ, from which we conclude, using Eq. (1), that $K/Y \sim 1/\gamma$. However, in Fig. 6 the face elasticity seems to follow a power law closer to -0.8 than -1. Perhaps residual stresses in the faces or on their boundaries are responsible for this difference.

V. CONCLUSIONS

In summary, we investigated the eigenvalue spectrum of a simple mass-and-spring model of a virus capsid as it passes through its buckling transition. The buckling of a spherical shell occurs in a smooth, nonsingular fashion, in contrast to the buckling of a disclinated planar network. The smearing can be attributed to symmetry breaking between the interior and exterior of the shell and is caused by the forbidden crossing of the buckling mode with a lower-frequency breathing mode.

Symmetries of the icosahedron and analogies with continuum-elastic theory were used to classify the normal modes. Modes of full icosahedral symmetry, transforming as the unit representation, soften as the Foppl–von Karman number passes through the buckling transition. Displacements during buckling, which resemble the maturation of real high-T-number virus capsids such as HK97, can be well represented as a superposition of the two lowest icosahedrally symmetric modes. A study using more realistic models [25] also showed that the lowest two modes were sufficient to describe maturation of HK97 and other high-T-number capsids. However, maturation of some small-T-number viruses (e.g., CCMV with $T = 3$) was well described using only the single lowest symmetric mode. In this case, if the value of γ is not too high, the deformation should be close to the $l = 0$ breathing mode, displacements should be nearly uniform across the shell, and the shape change minimal.

Susceptibilities to applied forces diverge at the buckling transition for planar networks. For spherical topology they evolve smoothly, with anomalies in the vicinity of γ_b. Susceptibility to forces applied at icosahedron vertices dominates near γ_b, but icosahedron edges and faces are much softer for large γ. In the limit of small γ, the effective spring constant approaches the behavior of a spherical continuum.

Beyond the buckling transition, the faces have the softest linear response, so this is where one might expect rupture in response to an isotropic osmotic pressure. The relative soft-

ness of icosahedron faces as compared to vertices has been reported experimentally in liposomes [4]. We verified this numerically by calculating the Q_6 parameter, which measures the distortion from a sphere to an icosahedron [5]. Below γ_b isotropic pressure weakly *increases* the value of Q_6, while above γ_b pressure strongly *decreases* Q_6, bending the facets to make the shape more nearly spherical.

[1] D. L. Caspar and A. Klug, Cold Spring Harbor Symp. Quant. Biol. **27**, 1 (1962).

[2] A. D. Dinsmore, M. F. Hsu, M. G. Nikolaides, M. Marques, A. R. Bausch, and D. A. Weitz, Science **298**, 1006 (2002).

[3] M. S. Spector, J. A. Zasadzinski, and M. B. Sankaram, Langmuir **12**, 4704 (1996).

[4] N. Delorme, M. Dubois, S. Garnier, A. Laschewsky, R. Weinkamer, T. Zemb, and A. Fery, J. Phys. Chem. B **110**, 1752 (2006).

[5] J. Lidmar, L. Mirny, and D. R. Nelson, Phys. Rev. E **68**, 051910 (2003).

[6] T. T. Nguyen, R. F. Bruinsma, and W. M. Gelbart, Phys. Rev. E **72**, 051923 (2005).

[7] G. A. Vliegenthart and G. Gompper, Biophys. J. **91**, 834 (2006).

[8] S. D. Hicks and C. L. Henley, Phys. Rev. E **74**, 031912 (2006).

[9] S. Timoshenko, *Theory of Plates and Shells* (McGraw-Hill, New York, 1940).

[10] A. E. H. Love, *A Treatise on the Mathematical Theory of Elasticity* (Dover, New York, 1944).

[11] F. I. Niordson, *Shell Theory* (North-Holland, Amsterdam, 1985).

[12] H. S. Seung and D. R. Nelson, Phys. Rev. A **38**, 1005 (1988).

[13] W. R. Wikoff, J. F. Conway, J. Tang, K. K. Lee, L. Gan, N. Cheng, R. L. Duda, R. W. Hendrix, A. C. Steven, and J. E. Johnson, J. Struct. Biol. **153**, 300 (2006).

[14] I. L. Ivanovska, P. J. de Pablo, B. Ibarra, G. Sgalari, F. C. MacKintosh, J. L. Carrascosa, C. F. Schmidt, and G. J. L. Wuite, Proc. Natl. Acad. Sci. U.S.A. **101**, 7600 (2004).

[15] W. S. Klug, R. F. Bruinsma, J.-P. Michel, C. M. Knobler, I. L. Ivanovska, C. F. Schmidt, and G. J. L. Wuite, Phys. Rev. Lett. **97**, 228101 (2006).

[16] F. Tama and C. L. Brooks, J. Mol. Biol. **318**, 733 (2002).

[17] T. A. Witten and H. Li, Europhys. Lett. **23**, 51 (1993).

[18] A. Lobkovsky, S. Gentges, H. Li, D. Morse, and T. A. Witten, Science **270**, 1482 (1995).

[19] B. A. DiDonna and T. A. Witten, Phys. Rev. Lett. **87**, 206105 (2001).

[20] B. A. DiDonna, Phys. Rev. E **66**, 016601 (2002).

[21] A. J. Wood, Physica A **313**, 83 (2002).

[22] T. A. Witten, Rev. Mod. Phys. **79**, 643 (2007).

[23] M. Widom, Phys. Rev. B **34**, 756 (1986).

[24] A. J. Rader, D. Vlad, and I. Bahar, Structure **13**, 413 (2005).

[25] F. Tama and C. L. Brooks, J. Mol. Biol. **345**, 299 (2005).

[26] H. W. T. van Vlijmen and M. Karplus, J. Mol. Biol. **350**, 528 (2005).

[27] M. A. Peterson, J. Math. Phys. **26**, 711 (1985).

[28] L. D. Landau and E. M. Lifshitz, *Theory of Elasticity* (Pergamon, Oxford, 1986).

[29] A. J. Levine and F. C. MacKintosh, Phys. Rev. E **66**, 061606 (2002); see also E. Frey and D. R. Nelson, J. Phys. I **1**, 1715 (1991).

[30] E. L. Hill, Am. J. Phys. **22**, 211 (1954).

[31] Handbook of Mathematical Functions, edited by M. Abramowitz and I. A. Stegun (Dover, New York, 1970).

[32] M. Tinkham, *Group Theory and Quantum Mechanics* (McGraw-Hill, New York, 1964).

[33] M. Buenemann and P. Lenz, Proc. Natl. Acad. Sci. U.S.A. **104**, 9925 (2007).